



**STUDY OF AFRICAN DUST WITH MULTI-WAVELENGTH RAMAN LIDAR DURING THE “SHADOW”  
CAMPAIGN IN SENEGAL**

I. Veselovskii<sup>1,2</sup>, P. Goloub<sup>3</sup>, T. Podvin<sup>3</sup>, V. Bovchaliuk<sup>3</sup>, Y. Derimian<sup>3</sup>, P. Augustin<sup>4</sup>, M. Fourmentin<sup>4</sup>, D. Tanre<sup>3</sup>, M. Korenskiy<sup>1</sup>, D.N. Whiteman<sup>5</sup>, A. Diallo<sup>6</sup>, T. Ndiaye<sup>6</sup>, A. Kolgotin<sup>1</sup>, O. Dubovik<sup>3</sup>

<sup>1</sup>*Physics Instrumentation Center of GPI, Troitsk, Moscow, 142190, Russia*

<sup>2</sup>*Joint Center for Earth Systems Technology, UMBC, Baltimore, MD, USA*

<sup>3</sup>*Laboratoire d'Optique Atmosphérique, Université de Lille-CNRS, 59650, Villeneuve d'Ascq, France*

<sup>4</sup>*Laboratoire de Physico-chimie de l'atmosphère, Université du littoral côte d'Opale, France*

<sup>5</sup>*NASA GSFC, Greenbelt, MD 20771, USA*

<sup>6</sup>*Institut de Recherche pour le Développement, Dakar, Sénégal*

1 **ABSTRACT**

2 West Africa and the adjacent oceanic regions are very important locations for studying  
3 dust properties and their influence on weather and climate. The SHADOW (Study of SaHaran  
4 Dust Over West Africa) campaign is performing a multi-scale and multi-laboratory study of  
5 aerosol properties and dynamics using a set of in situ and remote sensing instruments at an  
6 observation site located at IRD (Institute for Research and Development) Center, Mbour,  
7 Senegal (14°N, 17°W). In this paper, we present the results of lidar measurements performed  
8 during the first phase of SHADOW which occurred in March-April, 2015. The multiwavelength  
9 Mie-Raman lidar acquired  $3\beta+2\alpha+1\delta$  measurements during this period. This set of measurements  
10 has permitted particle intensive properties such as extinction and backscattering Ångström  
11 exponents (BAE) for 355/532 nm wavelengths corresponding lidar ratios and depolarization ratio  
12 at 532 nm to be determined. The mean values of dust lidar ratios during the observation period  
13 were about 53 sr at both 532 nm and 355 nm, which agrees with the values observed during the  
14 SAMUM 1 and SAMUM 2 campaigns held in Morocco and Cape Verde in 2006, 2008. The  
15 mean value of particle depolarization ratio at 532 nm was  $30\pm 4.5\%$ , however during strong dust  
16 episodes this ratio increased to  $35\pm 5\%$ , which is also in agreement with the results of the  
17 SAMUM campaigns. The backscattering Ångström exponent during the dust episodes decreased



1 to  $\sim -0.7$ , while the extinction Ångström exponent though being negative, was greater than  $-0.2$ .  
2 Low values of BAE can likely be explained by an increase in the imaginary part of the dust  
3 refractive index at 355 nm compared to 532 nm. The dust extinction and backscattering  
4 coefficients at multiple wavelengths were inverted to the particle microphysics using the  
5 regularization algorithm and the model of randomly oriented spheroids. The analysis performed  
6 has demonstrated that the spectral dependence of the imaginary part of the dust refractive index  
7 may significantly influence the inversion results and should be taken into account.

8

## 9 1. INTRODUCTION

10 The impact of desert dust emitted into atmosphere on the Earth's radiation budget is the  
11 subject of intense research (Sokolik and Toon, 1996; Balkanski et al., 2007; Mahowald et al.,  
12 2010; Formenti et al., 2011, 2014). Due to the wind patterns involved, dust can be transported  
13 far away from the main source regions in Africa and Asia allowing dust to be distributed in  
14 varying amounts all over the globe. North Africa is the largest source of dust in the world and  
15 several field campaigns have been conducted to evaluate dust particle microphysical properties  
16 over Western Africa and to study long range transport of Saharan dust (Reid et al., 2003; Tanre  
17 et al., 2003; Redelsperger et al., 2006; Haywood et al., 2008; McConnell et al., 2008). During  
18 these campaigns, dust particles were studied via aircraft, ground sampling and using sun  
19 photometer measurements. However, vertical distribution of dust has received little attention  
20 even though dust vertical structure is critical for an improved understanding of dust advection,  
21 transport and dust-cloud interactions. The commonly used instrument to evaluate the height  
22 profile of dust particle properties is the aerosol lidar. The numerous measurements performed in  
23 Europe, America and Asia with multiwavelength Raman and HSRL lidar systems have resulted  
24 in a significant amount of information about the vertical distribution of dust intensive properties,  
25 such as depolarization, lidar ratios, extinction and backscattering Ångström exponents (Sakai et al.,  
26 2003; De Tomasi et al., 2003; Shimizu et al., 2004; Mona et al., 2006; Papayannis et al.,  
27 2008; Xie et al., 2008; Ansmann et al., 2012; Burton et al., 2014; Nisantzi et al., 2015). However  
28 these measurements were mostly performed at a significant distance from the source area, so the  
29 dust particles were aged due to mixing with local aerosols and coating with soluble aerosol  
30 species (Li et al., 2009) and may not have well represented the characteristics of the dust upon  
31 initial emission.



1           To analyze the properties of pure dust measurements near the source regions are needed.  
2   Such measurements of Saharan dust were performed during the SAMUM1 and SAMUM2  
3   experiments using the assembly of Raman and HSRL lidars (Ansmann et al., 2011). During  
4   those measurements the dust episodes and more complicated events, when the dust and smoke  
5   layers occurred simultaneously, were studied (Tesche et al., 2009a,b; 2011; Esselborn et al.,  
6   2009). However, for the estimation of aerosol radiative forcing not only the particle intensive  
7   parameters, but also their microphysical properties, such as size, concentration and the complex  
8   refractive index (CRI) are needed. An estimation of the vertical distribution of particle  
9   microphysics can be achieved, for example, by combining lidar and sun photometer  
10   measurements; a review of such studies can be found in a recent publication (Biniotoglou et al.,  
11   2015). However in these retrievals the mean radii and refractive indices of particles in the fine  
12   and the coarse mode are assumed to be height independent, and only particle volume in each of  
13   the modes is permitted to vary. Such assumptions may become invalid when aerosol layers of  
14   different origins occur.

15           The alternative approach to evaluating the vertical distribution of dust properties is to  
16   estimate the particle properties from lidar measurements only. Raman (or HSRL)  
17   multiwavelength lidars based on a tripled Nd:YAG laser are able to provide three particle  
18   backscattering and two extinction coefficients (so called  $3\beta+2\alpha$  dataset). Different techniques  
19   have been considered to invert these measurements into particle microphysics (Ansmann and  
20   Müller, 2005), but the main issue is small number of input measurements (typically five),  
21   compared to the numerous parameters needed for describing the aerosol microphysical  
22   properties. This implies that the inverse problem is underdetermined and that numerous solutions  
23   may reproduce the input measurements with similar accuracy. This family of solutions can be  
24   localized by applying constraints to the "search space", i.e. limiting the range of particle radii and  
25   refractive indices considered. The additional assumption usually made is that the refractive index  
26   is spectrally independent and identical over the whole size range (Müller et al., 1999;  
27   Veselovskii et al., 2002). Such an approach has proved to be efficient for aerosol particle size  
28   distributions (PSD) with a predominant fine mode as, for example, in the case of biomass  
29   burning aerosols (Müller et al., 2005; Veselovskii et al., 2015). However, in the case of dust the  
30   inversion of lidar measurements becomes more challenging since the dust PSD contains a strong  
31   coarse mode with particle radii extending up to  $\sim 15 \mu\text{m}$  and the estimation of properties for such



1 big particles is less accurate when measurements are only performed in the wavelength range of  
2 355-1064 nm. Moreover, dust particles are of irregular shape and Mie theory is thus not  
3 applicable for computations of their scattering properties. Also, the imaginary part of the  
4 refractive index (RI) of dust is spectrally dependent, with a strong enhancement of the absorption  
5 in the UV region (Patterson et al., 1977). And finally, particles in the fine and coarse mode may  
6 have different origin, so the size dependence of the refractive index should also be considered.  
7 The complexity of the problem outlined above demands the use assumptions and  
8 simplifications in the retrieval algorithms.

9 A widely used model for treating irregularly shaped particles is the one used in the  
10 operational AERONET algorithm that mimics dust scattering properties with an assembly of  
11 randomly oriented spheroids (Mishchenko et al., 1997; Dubovik et al., 2006). For typical dust  
12 PSDs the AERONET model provides lidar and depolarization ratios which agree reasonably  
13 well with observed values (Wiegner et al., 2009; Esselborn et al., 2009; Tesche et al., 2009b).  
14 The first attempts to invert lidar dust measurements into particle microphysics using the  
15 spheroids model were recently made (Veselovskii et al., 2010; Di Girolamo et al., 2012;  
16 Papayannis et al., 2012) but were applied to lofted layers of aged dust over Europe. The only test  
17 of the spheroidal model relevant to pure dust was performed by using the data acquired during  
18 the SAMUM-1 and SAMUM-2 campaigns (Müller et al., 2013). Results indicate that the  
19 effective radii derived from lidar measurements are in reasonable agreement with the values  
20 provided by AERONET and airplane sampling, while differences are significant for the  
21 refractive index.

22 The application of spheroids to the analysis of lidar dust observations is an important step  
23 forward when compared to the spherical particle approximation of Mie theory. Still we should  
24 keep in mind that spheroid model was not specifically designed for lidar applications where  
25 scattering in the backward direction is considered. For instance, as previously discussed  
26 (Gasteiger et al., 2011; Müller et al., 2013) the spheroidal model has difficulty in reproducing  
27 depolarization ratios ( $\delta$ ) greater than 30%, values that are representative for pure dust. When  
28 using the spheroidal model, such high depolarization ratios can only be obtained when the real  
29 ( $m_R$ ) and imaginary ( $m_i$ ) parts of the refractive index are less than 1.5 and 0.005, respectively  
30 (Dubovik et al., 2006), even though coincident in situ measurements of dust report higher values



1 (Kandler et al., 2011). To investigate these issues, more measurements near the dust origin  
2 source and more tests of suitable inversion schemes are needed.

3 West Africa and the adjacent oceanic regions are very important locations for studying  
4 dust properties and their influence on weather and climate. The SHADOW (Study of SaHaran  
5 Dust Over West Africa) campaign is performing a multi-scale and multi-laboratory study of  
6 aerosol properties and dynamics using a set of in situ and remote sensing instrumentation (multi-  
7 wavelength Raman LIDAR, Wind-LIDAR, nephelometer, aethalometer, sun/lunar photometer,  
8 airborne sunphotometer, optical particle counter) in the framework of the CaPPA (Chemical and  
9 Physical Processed in The Atmosphere) project (<http://www.labex-cappa.fr/>). The site is located  
10 at IRD (Institut for Research and Development) Center, Mbour, Senegal (14<sup>0</sup>N, 17<sup>0</sup>W). The  
11 objective of the experiment is to report the optical, chemical and physical properties of the  
12 aerosols as well as the source apportionment in a location where aerosol loading can be very  
13 large and aerosol type depends on the season. Two enhanced observing periods of 7 weeks are  
14 considered: March-April 2015 when dust originating from the Sahara/Sahel region is dominant  
15 and December 2015-January 2016 when dust and carbonaceous aerosols resulting from fire  
16 activities are in variable proportion and transported at different altitudes. Other types of aerosols  
17 can also be present such as sulfates from nearby urban areas or maritime aerosols depending on  
18 the air mass flow. The mixed state of these various chemical components results in different  
19 radiative properties of the aerosols.

20 We hereinafter focus our study on multiwavelength Mie-Raman lidar measurements  
21 performed during the first phase of the SHADOW campaign for the period 8 March - 24 April.  
22 During this period approximately 40 day- and night-time measurement sessions were performed  
23 and numerous strong dust episodes were observed. Those lidar observations are used for the  
24 analysis of the vertical distribution of the dust intensive and microphysical properties. In section  
25 2 we describe the lidar equipment and in section 3 we provide examples of joint measurements  
26 of wind and Raman lidars. Section 4 presents day-to-day variation of dust properties and  
27 examples of vertical distribution of dust intensive parameters. The results of inversion of lidar  
28 measurements into particle microphysics are given in section 5.

29

30

31 **2. LIDAR EXPERIMENTAL SET**



1 Data from three lidar systems were available during SHADOW campaign. These systems  
2 are: aerosol micropulse lidar, wind lidar and multiwavelength Mie-Raman lidar.

### 3 *Aerosol micropulse lidar*

4 Cimel CE-370 micropulse lidar ([www.cimel.fr](http://www.cimel.fr)) was operated 24 hours per day at 532 nm  
5 wavelength allowing real-time monitoring of aerosol layer stratification. After correction for the  
6 geometrical overlap factor, the lidar provides range corrected co- and cross polarized lidar  
7 signals for heights above 300 m.

### 8 *Doppler lidar*

9 The wind field within the lower troposphere (<5 km) was measured by an eye safe  
10 scanning wind lidar (Windcube WLS 100) manufactured by the LEOSPHERE company  
11 ([www.leosphere.com](http://www.leosphere.com)). This pulsed Doppler lidar operates at 1543 nm with a repetition rate of 10  
12 kHz and uses a heterodyne technique to measure the Doppler shift of laser radiation  
13 backscattered by aerosols. Simultaneous measurements of radial wind speed and aerosol  
14 backscatter provides information on both aerosol layer stratification and the dynamics of the  
15 lower troposphere (Thobois and Soderholm, 2015). More technical details are given by (Kumer  
16 et al., 2014; Ruchith and Ernest Raj, 2015).

17 During this experiment, continuous monitoring of the wind field in the range from 100 m  
18 to 5 km with 50 m range resolution was performed. The total scanning cycle included two 180°  
19 scans in the vertical plane along East/West and South/North axes with 1° resolution, 360°  
20 azimuthal scan with 2° resolution at 5° elevation angle, and line of sight (LOS) profiles at 75°  
21 elevation in the four cardinal directions. The duration of the total cycle was approximately 10  
22 minutes. The combination of LOS sequences is used in order to determine the three components  
23 of the wind vector vertical profile relying on the Doppler Beam Swinging (DBS) technique  
24 (Browning and Wexler, 1968).

### 25 *Multiwavelength Mie-Raman lidar*

26 The LILAS multiwavelength Mie-Raman lidar is based on a tripled Nd:YAG Spectra  
27 Physics INDI laser with a 20 Hz repetition rate, and pulse energy of 90/100/100 mJ at  
28 355/532/1064 nm. The backscattered light is collected by a 40-cm aperture Newtonian  
29 telescope, which is inclined at an angle of 47 degrees to the horizon. The outputs of the detectors  
30 are recorded at 7.5 m range resolution using Licel transient recorders that incorporate both  
31 analog and photon-counting electronics. The full geometrical overlap of the laser beam and the



1 telescope FOV is achieved at 800 m -1400 m range depending on FOV used. The system is  
2 designed for simultaneous detection of elastic and Raman backscatter signals and thus provides  
3 three particle backscattering and two extinction coefficients along with depolarization ratio at  
4 532 nm (so called  $3\beta+2\alpha+1\delta$  set). For the calibration of depolarization measurements, the so  
5 called  $\pm 45^\circ$  method, (Freudenthaler et al., 2009) was used. The uncertainty of depolarization  
6 measurements due to calibration is estimated as  $\pm 15\%$ . Acquiring Raman backscatter at 408 nm  
7 permits profiling the water vapor mixing ratio (WVMR) (Whiteman et al., 1992). For calibration  
8 of the WVMR, radiosonde launches from the Dakar airport, located  $\sim 70$  km from Mbour, were  
9 used. The large separation between the lidar and radiosonde locations prevented an accurate  
10 calibration of the WVMR so the WVMR data were used mainly to monitor the relative change of  
11 the water vapor content. To improve the system capability for particle extinction measurements  
12 at 532 nm, rotational Raman (RR) scattering was used instead of vibrational nitrogen Raman  
13 scattering at 608 nm (Veselovskii et al., 2015). For each profile, 4000 laser pulses were  
14 accumulated so the temporal resolution of the measurements was approximately 3 minutes.

15

### 16 3. TROPOSPHERE STRATIFICATION AND DYNAMICS

17 The aerosol layer stratification over the observation site was mixed-up and difficult to  
18 analyze. To demonstrate the advantage of the joint use of wind and Raman lidar measurements,  
19 we provide an example of observations performed on the night of 15-16 April. The transport  
20 paths of different stratified air masses have been studied by using back trajectories from the  
21 NOAA HYSPLIT model (<http://ready.arl.noaa.gov/HYSPLIT.php>).

22 For period from 23:00 UTC to 7:00 UTC on 15-16 April night, the time-height sections  
23 of the logarithmic range corrected signal (LRCS) is shown in fig.1 while fig.2 shows the  
24 horizontal wind speed (color scale) and direction (arrow) deduced from wind lidar and the sonic  
25 anemometer wind measurements near the ground. Back trajectories of the air masses ending in  
26 Mbour on 16 April 2015 at 2500 m (02:00 UTC, 06:00 UTC), at 900 m (00:00 UTC) and at 700  
27 m (06:00 UTC) are reported in Fig.3. These figures reveal complex stratification and dynamics  
28 of the lower troposphere on 15-16 April: we can distinguish four layers (A-D) from 100 m to a  
29 height of approximately 3000 m. In parallel, the wind field highlights the appearance of multi-  
30 layered wind structure mainly consisted of a northerly wind (downward arrow) prevailing near  
31 ground, which changes to an easterly wind (leftward arrow) with height (fig. 2).



- 1 • Layer A, located between 1000 m to 3000 m (at 00:00 UTC), is associated with a small  
2 northerly wind speed ( $< 5$  m/s) in the lower part of the layer, and a slightly larger easterly  
3 wind speed ( $> 5$  m/s) above 2000 m. Layer A can be considered to be a continentalized  
4 maritime trade (CMT) wind which is one of oceanic origin that has been progressively  
5 altered by continental trade (CT), as follows from the back trajectories shown in fig.3.  
6 Therefore, this layer is characterized by a mixture of maritime and continental air.
- 7 • Layer B located between 400 m - 800 m at the beginning of the study period rises  
8 progressively up to 700 m - 1000 m by the end of the dataset. This layer is characterized by  
9 northeasterly winds and high aerosol loading. According to the back trajectories shown in  
10 fig. 3, this air mass was transported from a continental area (Mali) and was mainly advected  
11 by a southeasterly continental wind (CW).
- 12 • Layer C is a nocturnal low-level jet (LLJ). The jet core height is between 250 and 400 m  
13 with a maximum jet speed exceeding 15 m/s. The LLJ was observed throughout the night  
14 with a thickness that progressively increased with time perhaps being the causative  
15 mechanism for the corresponding increase in height of layer B (fig.1). The LRCS values  
16 within layer C decrease progressively up to the end of the observation period, perhaps due to  
17 dilution of the aerosol loading.
- 18 • Finally, layer D corresponds to the nocturnal boundary layer (NBL) characterized by high  
19 LRCS values and by small northerly or northwesterly wind speed ( $< 5$  m/s). The NBL top  
20 can be deduced from the LRCS profile discontinuity (Seibert et al., 2000) and is estimated to  
21 at a height of approximately 200-300 m during the night.

22 Fig.4 shows the particle extinction at 532nm (4-a), water vapor mixing ratio (4-b), lidar  
23 ratio (4-c) and depolarization ratio (4-d) both at 532 nm for the same time-height section as in  
24 fig. 1 and 2. The water vapor can be used as a convenient tracer to separate dry continental air  
25 masses from oceanic air masses that are characterized by higher vapor content. Due to the  
26 geometrical overlap factor, the LILAS minimum height of the measurements shown in fig 4 is  
27 800 m. Still, layer B (CW) is well observed starting at 03:00 UTC (fig.4a) due to the increase of  
28 the layer height. The particle extinction  $\alpha_{532}$  in layer A increases after 03:00 UTC while the  
29 mixing ratio is decreasing (fig.4b). This may indicate that continental air mass advected by CT  
30 has become dominant. The lidar ratio  $LR_{532}$  of the particles associated with CT is about 55 sr



1 while for CMT as observed during the first part of the observation period, it is lower. The  
2 depolarization ratio  $\delta_{532}$  is about 30% in layer A and shows a small enhancement up to 35% for  
3 layer B.

4

#### 5 **4. DUST PARTICLE PROPERTIES DERIVED FROM RAMAN LIDAR**

##### 6 **OBSERVATIONS**

###### 7 *4.1. Day-to-day variation of particle intensive parameters*

8 One of the goals of the SHADOW campaign was to study the dust particle intensive  
9 parameters such as extinction and backscattering Angstrom exponents together with lidar and  
10 depolarization ratios. During March-April 2015 about 40 measurement sessions, including both  
11 day and night time periods, were performed. In the analysis presented below only night time  
12 measurements are considered, and for every session all lidar signals measured during the night  
13 are temporally averaged. Moreover, for an evaluation of day-to-day variations of the particle  
14 parameters we use only extinction and backscattering coefficients averaged within 1500 – 2000  
15 m height layer, where a high dust concentration is frequently observed. In addition, only  
16 observations with particle depolarization above 20% are selected to guarantee major dust  
17 contribution.

18 To give an overview of the variation in aerosol loading, the aerosol optical thickness  
19 (AOT) at 440 nm together with the extinction Angstrom exponent (EAE)  $A_{380/500}^{\alpha}$  measured with  
20 Cimel sun photometer is reported in Fig.5 for the 10 March-23 April 2015 period. The AOT was  
21 relatively low (mainly below 0.4) for 17-28 March, but increased after 28 March reaching values  
22 up to 2.0. The high AOTs are associated with low values of the extinction Angstrom exponent  
23 indicating numerous dust episodes. Fig.6 shows the particle extinction  $\alpha_{532}$  together with  
24 extinction (EAE) and backscattering (BAE) Angstrom exponents  $A_{355/532}^{\alpha}$ ,  $A_{355/532}^{\beta}$  derived from  
25 the lidar measurements for the same time period. During 28 March – 15 April several strong dust  
26 episodes occurred as indicated by averaged over night particle extinction values as high as 0.5  
27  $\text{km}^{-1}$ . The insert in fig.6 provides the frequency distribution of observed EAE and BAE values.  
28 Typically EAE varies in 0-0.3 range, but during dust episodes the values of EAE became  
29 negative, decreasing to  $\sim -0.15$ . The BAE averaged over night presents stronger variation,



1 because it is more sensitive to the change of complex refractive index (CRI) and decreases to a  
2 low a value as -0.55 during dust events.

3 The day-to-day variation of the lidar ratios at 355 nm and 532 nm together with particle  
4 depolarization ratio at 532 nm is shown in fig.7. The lidar ratios at both wavelengths vary in the  
5 40–65 sr range and the frequency distribution for the ratio  $LR_{355}/LR_{532}$  is given by insert in fig.7.  
6 In 60% of the cases the ratio  $LR_{355}/LR_{532}$  is close to 1, but during dust events this ratio increased  
7 up to 1.4. The mean values of lidar ratios are close:  $LR_{355}=54\pm 8$  sr and  $LR_{532}=53\pm 8$  sr. The  
8 mean value of particle depolarization ratio is  $30\pm 4.5\%$ , however during the dust events  
9 depolarization ratio could increase up to  $35\pm 5\%$ .

#### 10 **4.2. Vertical distribution of particle intensive properties**

11 The vertical distribution of particle intensive properties is strongly influenced by the  
12 origin of the air masses which during the SHADOW measurement period were coming either  
13 from ocean or continental regions. In this section, we present the results for three days (13, 29  
14 March and 10 April) characterized by different types of air masses.

##### 15 **13 March**

16 As follows from fig.8, on 13 March at 21:00 UTC the air masses at the 3 heights (1500,  
17 2500 and 3500m) were transported mainly over the ocean, but the back trajectory at 1500 m  
18 presents a “loop” over continent, so the corresponding air masses may contain more dust  
19 compared to other heights. Fig.9 shows the vertical profiles of  $3\beta+2\alpha$  measurements together  
20 with lidar ratios  $LR_{355}$ ,  $LR_{532}$ , depolarization ratio  $\delta_{532}$ , and Angstrom exponents  $A_{355/532}^{\alpha}$ ,  $A_{355/532}^{\beta}$   
21 on 13 March 2015 averaged over the 20:30–21:30 time period. The aerosol layer extended up to  
22 3500 m but the extinction coefficient  $\alpha$  was relatively small; at both 355 and 532 nm  
23 wavelengths  $\alpha$  did not exceed  $0.16 \text{ km}^{-1}$ . The particle depolarization ratio at 532 nm was  
24 approximately  $31\pm 4.5\%$  inside the dust layer (up to  $\sim 2750$  m) and decreased to less than 15% at  
25 3250 m. Likewise, the  $A_{355/532}^{\alpha}$  and  $A_{355/532}^{\beta}$  are close to zero up to 2750 m, but start to increase  
26 above indicating the presence of smaller particles. The lidar ratios  $LR_{355}$  and  $LR_{532}$  are  
27 approximately  $53\pm 8$  sr inside the dust layer. Above 2750 m the values of LR are more noisy but  
28 do not seem to change.

##### 29 **29 March**



1           The backtrajectories from the night of 29-30 March associated to a strong dust case are  
2 shown in Fig.10. The air masses at low altitude were transported over the continent and were  
3 strongly loaded with dust. Fig.11 presents the vertical profiles of the same particle parameters as  
4 in fig.10 but for 29 March. The extinction coefficient  $\alpha$  inside the dust layer (below 1500 m) is  
5 greater than  $0.6 \text{ km}^{-1}$  for both wavelengths. The backscattering coefficient  $\beta_{355 \text{ nm}}$  inside the dust  
6 layer is lower than  $\beta_{532}$  which is consistent with the lidar ratio  $R$  larger at 355 nm than that at 532  
7 nm with values as large as 65 sr. The  $A_{355/532}^{\beta}$  (BAE) is negative and gets near -0.8, while EAE is  
8 still close to 0 as observed on 13 March (Fig.9). The negative values of BAE can result from the  
9 spectral dependence of the imaginary part of the dust refractive index (RI) which is larger at 355  
10 than at 532 nm (e.g. Patterson et al., 1977; Ansmann et al., 2011).

11           The ground based measurements performed during the SAMUM campaign demonstrated  
12 that the imaginary part of the dust RI could vary from  $m_i=0.005$  at 532 nm to  $m_i=0.02$  at 355 nm  
13 (Ansmann, et al., 2011). Such a strong enhancement of  $m_i$  may lead to a decrease of the  
14 backscattering coefficient (Veselovskii et al., 2010). To estimate the impact of the  $m_i$   
15 enhancement at 355 nm on the values of EAE and BAE at 355/532 nm wavelengths, numerical  
16 simulations were performed. Extinction and backscattering Ångström exponents were calculated  
17 using the model of randomly oriented spheroids as described in (Veselovskii et al., 2010) for a  
18 bimodal particle size distribution:

$$19 \quad \frac{dn(r)}{d \ln(r)} = \sum_{i=f,c} \frac{N_i}{(2\pi)^{1/2} \ln \sigma_i} \exp \left[ -\frac{(\ln r - \ln r_i)^2}{2(\ln \sigma_i)^2} \right] \quad (1)$$

20 where  $N_{f,c}$  is particle number density in the fine ( $f$ ) and the coarse ( $c$ ) mode. Each mode is  
21 represented by a lognormal distribution with modal radius  $r_{f,c}$  and dispersion  $\ln \sigma_{f,c}$ . For the  
22 fine mode, values of  $r_f=0.1 \mu\text{m}$  and  $\ln \sigma_f=0.4$  were used. For the coarse mode  $r_c=1.0 \mu\text{m}$  and  
23 three values  $\ln \sigma_c=0.4, 0.5, 0.6$  were considered. The three size distributions expressed in  
24 volume are reported in the insert of fig.12. The ratio  $N_c/N_f$  in all cases was 0.01, and the real part  
25 of CRI was 1.55 for all wavelengths. The imaginary part was fixed at 0.005 for 532 nm while it  
26 varied within the 0.005 – 0.05 range at 355 nm. Values of EAE and BAE as a function of  $m_i$  at  
27 355 nm are given by fig.12. The EAE shows no significant sensitivity to changes in  $m_i$ , but BAE



1 decreases rapidly as a function of  $m_I$  at 355 nm. The present sensitivity study is limited but  
2 illustrates the importance of accounting for the right spectral dependence of  $m_I(\lambda)$ .

### 3 **10 April**

4 On April 10, the air masses were coming from continental regions and particle  
5 parameters showed large variation with height. We selected measurements during the period  
6 0:00-2:00 UTC for which the backward trajectories at 1:00 UTC are shown in fig.13. The air  
7 masses at 2000 m and 3000 m originate from the dust-laden continental region (Barren or  
8 sparsely vegetated areas), while at 4500 m the air masses come from regions covered by grass  
9 lands and savannas. Fig.14 shows profiles of the  $3\beta+2\alpha$  measurements together with particle  
10 intensive parameters. The particle extinction increases with height reaching a maximum value of  
11 around  $0.2 \text{ km}^{-1}$  for both wavelengths at a height of 3000 m and then decreases up to 5 000m.  
12 The EAE is approximately zero up to 3000 m and then it increases to 1.0 at 4500 m. The BAE  
13 below 3000 m is smaller with minimum value  $A_{355/532}^{\beta} \approx -0.5$ , but increase up to 4500 m where  
14 EAE and BAE are approximately equivalent. The depolarization ratio is around 30% in the  
15 2000-3500 m range, and decreases for higher altitudes. So we can identify different aerosol  
16 layers with different properties: mostly pure dust layer within the 2000-3500 m altitude range  
17 and mixed aerosols above it.

18 The relative humidity on 10 April was higher than on 13, 29 March, which could impact  
19 the particle properties. Fig.15 shows the estimated profile of water vapor mixing ratio (WVMR)  
20 obtained from the lidar measurements. WVMR is less than 3 g/kg within the dust layer and  
21 increases above 3500 m reaching approximately 5.5 g/kg at 4000 m. The WVMR and the  
22 relative humidity measured in Dakar at 0:00h using a radiosounding is reported on Fig.15 for  
23 comparison. Both WVMR's measured by sounding and lidar are in agreement between 3000m  
24 and 5000m (note that there is no sounding data between 4620 m and 3880 m). There are clearly  
25 two distinct layers. If the derived properties of aerosols within the lower layer are representative  
26 of dust, the air mass above 4000m brings another particle type. Particles, characterized by lower  
27 depolarization ratio, are smaller since the EAE is increasing, and the layer is more humid since  
28 the RH is increasing. Based on the analysis of the satellite data quick-looks (see for instance  
29 <http://earthobservatory.nasa.gov/GlobalMaps/>), the back-trajectories reporting in Fig. 13 show  
30 that the air mass at 4500m is coming from regions where fires were active during several days,



1 which can result in emission of smoke particles transported over M'Bour few days later. The  
2 derived properties of aerosols within the 4000-5000m layer are consistent with this hypothesis;  
3 the assumption of the air-mass origin is also consistent with the RH increase.

4

## 5 **5. INVERSION OF RAMAN LIDAR OBSERVATIONS TO THE PARTICLE** 6 **MICROPHYSICS**

7 The lidar  $3\beta+2\alpha$  and  $3\beta+2\alpha+1\delta$  observations analyzed in the previous sections can be  
8 inverted into microphysical properties using regularization algorithm. As previously mentioned,  
9 in the case of irregularly shaped dust particles such inversion is more complicated compared to  
10 other aerosol types that may be well handled by spherical particle assumptions. In an earlier  
11 study, a model of randomly oriented spheroids for dust was used (Veselovskii et al., 2010). This  
12 model handles the dust particles as a mixture of spheres and spheroids, so an additional unknown  
13 parameter, spheroids volume fraction (SVF), appears. The SVF in principle can be determined in  
14 the process of inversion of  $3\beta+2\alpha+1\delta$  measurements thanks to the use of depolarization ratio as  
15 input parameter. However, for the dust layers, in a first guess, we assume a value of SVF=100%  
16 to decrease the number of retrieved parameters. In the process of inversion we used the “search  
17 space” parameters similar to those described in (Müller et al., 2013). The boundary of the  
18 inversion window has been set to minimum and maximum particle radii of 0.075 and 15  $\mu\text{m}$ ,  
19 respectively. The real part of RI was allowed to vary in the range 1.35 - 1.65, while the  
20 imaginary part varied in the range 0 - 0.02. The refractive index was assumed to be spectrally  
21 independent. The effects of a possible spectral dependence of the imaginary part of RI will be  
22 considered at the end of this section.

23 Fig. 16 shows the particle volume density retrieved from  $3\beta+2\alpha$  measurements on 13  
24 March, 29 March and 10 April, which were discussed in the 4.2 section. The profiles of particle  
25 volume are given together with corresponding extinction coefficients at 532 nm. The volume –  
26 extinction ratio  $V/\alpha_{532}$  for these days is also reported as an insert. Inside the dust layer this ratio  
27 varies within the range  $(0.50-0.65)\cdot 10^{-6}$  m, while outside the dust layer, the  $V/\alpha_{532}$  ratio  
28 decreases. An overview of observed values of the volume – extinction ratio for dust, obtained  
29 from in situ, AERONET and lidar measurements is presented in Ansmann et al., 2012 and  
30 provides  $V/\alpha_{532}$  varying within the range  $(0.60-1.29)\cdot 10^{-6}$  m. Thus our results are near the low  
31 boundary of these previously published results.



1

2           The profiles of the effective radius and the real part of RI are shown in fig.17. The  
3 inverted effective radius inside the dust layer is between 1.05 and 1.25 $\mu\text{m}$  (1.15 $\pm$ 0.3  $\mu\text{m}$ ) and  
4 similar for the 3 days. The AERONET retrievals provided column integrated values that are in  
5 the same range and agrees within the uncertainty. On 30 March early morning, when the dust  
6 contribution to the AOT is prevailing, the effective radius  $r_{\text{eff}}=1.36 \mu\text{m}$  and it varies between  
7 0.918 and 1.70 depending on the days and time. The lidar retrievals indicate that the real part of  
8 the CRI in the dust layer varied from 1.51 $\pm$ 0.05 to 1.57 $\pm$ 0.05, which is quite typical for desert  
9 dust (Patterson et al., 1977), while the AERONET retrievals yield values between approximately  
10 1.46 and 1.58 depending on the days. Outside of the dust layer the retrieval of  $m_R$  is not reliable  
11 because the assumption of SVF=100% is not fulfilled and, as a result, the retrieved values of  $m_R$   
12 are overestimated (Veselovskii et al., 2010).

13           The values of the imaginary part of the CRI retrieved from lidar measurements are  
14 approximately 0.007 inside the dust layer. However, the retrieved value is unreliable since  
15 associated to high uncertainties (Müller et al., 2013) and, in addition, influenced by the  
16 assumption of a spectrally independent value.

17           The regularization approach provides the main features of the particle volume size  
18 distribution (PSD). Fig.18 shows the PSDs derived from lidar measurements on 10 April for four  
19 height layers of 150 m width centered at 1940, 3150, 4070, 4370 m heights. For the layers with  
20 strong dust loadings (1940, 3150 m) the coarse mode is dominant, at higher altitude outside the  
21 dust layer (4070, 4370 m), the fine mode (around 0.15 $\mu\text{m}$ ) prevails. For comparison, the column  
22 integrated PSD obtained from AERONET level 1.5 data on 9 April at 18:00 UTC is also  
23 reported. The coarse mode looks shifted toward larger particles when compared to the lidar  
24 retrievals but the difference can be due to the spectral dependence of the imaginary part of  $m_I$ , as  
25 it will be discussed further in this section.

26           Depolarization measurements provide additional information about particle properties  
27 that can be used in the inversion algorithm as long as the forward model can compute the particle  
28 depolarization ratio with sufficient accuracy (Veselovskii et al., 2010; Müller et al., 2013).  
29 Hereinafter, we compare the retrieved aerosol parameters using  $3\beta+2\alpha$  or  $3\beta+2\alpha+1\delta$   
30 observations. To perform such a comparison we calculated the ratio of the effective radii ( $R_g^r$ )



1 derived from  $3\beta+2\alpha+1\delta$  and  $3\beta+2\alpha$  sets. Fig.19 shows the profiles of  $R_{\delta}^r$  for the same three days  
2 (right part associated with bottom x-axis); a value of 1.0 would mean that the additional input  
3 has no impact on the retrieval. Inside the dust layer the ratio is about 1.15 for the measurements  
4 taken on 13 and 29 of March. On 10 April, the ratio is noisier and more oscillating, but the  
5 average is still close to the results obtained for 13 and 29 March. Let us mention that the ratio of  
6 the particle volumes  $R_{\delta}^V$  is very close to  $R_{\delta}^r$ , so it is not shown in the figure. The increase of the  
7 effective radius (and volume) retrieved from  $3\beta+2\alpha+1\delta$  measurements compared to  $3\beta+2\alpha$   
8 occurs simultaneously with a decrease of the real and imaginary parts of CRI (Veselovskii et al.,  
9 2010; Müller et al., 2013).  $m_R$  and  $m_I$  decrease to values less than 1.45 and 0.005, respectively  
10 and are lower than expected based on in situ measurements (Müller et al., 2013). It may suggest  
11 that the spheroidal model has difficulty to reproduce high depolarization measurements. On  
12 March 13 and April 10, the depolarization ratio  $\delta$  is decreasing above 2500m and 3700m (Figs 9  
13 and 14 respectively) and we can notice that the value  $R_{\delta}^r$  is then close to 1. Assuming that results  
14 obtained using  $3\beta+2\alpha$  data are more representative of the actual values, it means that the  
15 spheroidal model cannot reproduce high depolarization ratios reasonably well. Additional  
16 information brought by the depolarization ratio is so not suitable in such conditions.

17 The inversion results presented in fig.16, 17 are obtained assuming a spectrally  
18 independent refractive index while the imaginary part of CRI of dust is expected to increase in  
19 the UV spectral region. To test the effect of a spectrally dependent imaginary part  $m_I(\lambda)$  on the  
20 retrieval, we now assume that the imaginary parts at 1064 nm and 532 nm wavelengths are the  
21 same  $m_I(532) = m_I(1064)$ , while  $m_I(355) = 4m_I(532)$ . Such an enhancement of  $m_I$  at 355 nm is  
22 quite typical for Saharan dust (Ansmann et al., 2011). The  $3\beta+2\alpha$  measurements for the same  
23 three days are so inverted assuming this  $m_I(\lambda)$  spectral dependence as described in (Veselovskii  
24 et al., 2010). Fig.19 (left part associated with top x-axis) shows profiles of  $R_{m_I}^r$ , which is the  
25 ratio of the effective radii retrieved under the assumption of spectrally dependent and spectrally  
26 independent imaginary part of RI. Again, the corresponding ratios  $R_{m_I}^V$  for the volumes are close  
27 to  $R_{m_I}^r$  and we do not report them. As expected, the effect of  $m_I(\lambda)$  is more pronounced inside the  
28 dust layer, and on 29 March and 10 April (days characterized by negative BAE), the value of  
29  $R_{m_I}^r$  is up to 1.5. These model computations demonstrate that accounting for the spectral



1 dependence of the imaginary part of RI in the dust layers may significantly increase the retrieved  
2 values of the effective radius and particle volume. In particular, it may explain smaller radii of  
3 the coarse mode particles retrieved from lidar measurements inside the dust layer (fig.19) when  
4 compared to AERONET results.

5

## 6 CONCLUSION

7 The lidar measurements performed in March-April 2015 during the first phase of the  
8 SHADOW campaign in Senegal has provided a significant amount of information about dust  
9 particle parameters. The use of rotational Raman scattering in the LILAS for 532 nm  
10 observations improved the  $\alpha_{532}$  measurements and, as a result, the calculation of lidar ratio and  
11 extinction Angstrom exponent were improved as well. The mean values of lidar ratios of pure  
12 dust were about  $53 \pm 8$  sr for both 532 nm and 355 nm wavelengths, which agrees with the values  
13 observed during SAMUM 1 (Morocco) and SAMUM 2 (Cape Verde) campaigns. The mean  
14 value of particle depolarization ratio at 532 nm was  $30 \pm 4.5\%$ , however during strong dust  
15 episodes this ratio increased up to  $35 \pm 5\%$ , which is also in agreement with the results of  
16 SAMUM campaigns. The backscattering Angstrom exponent at 355/532 nm wavelengths during  
17 the dust episodes decreased to  $\sim -0.7$ , while the EAE values, though being negative, were higher  
18 than  $-0.2$ . Low values of BAE may be a result of enhanced dust absorption at 355 nm.

19 The inversion of  $3\beta+2\alpha$  measurements to particle microphysics in the case of dust is more  
20 challenging than other types of aerosols. The use of pure dust observations somehow simplifies  
21 this task, because the contribution of the particles in the fine mode (which may have different  
22 origin) is insignificant. Moreover, in the retrieval of pure dust properties we don't need to  
23 consider the mixture of spheres and spheroids and can assume SVF=100%. The use of the  
24 spheroids model for the inversion of  $3\beta+2\alpha$  measurements leads to values of effective radius in  
25 reasonable agreement with AERONET observations and yields reasonable values of the real part  
26 of RI. However, the use of depolarization measurements ( $3\beta+2\alpha+1\delta$ ) in the inversion for pure  
27 dust, which is characterized by a depolarization ratio  $\delta_{532}$  exceeding 30%, leads to values of  
28 effective radius and volume exceeding the corresponding values obtained from  $3\beta+2\alpha$   
29 measurements by a factor up to 1.15. At the same time, the values of  $m_R$  are decreased. These  
30 issues have already been discussed so at the current time we prefer to not use the depolarization  
31 ratio in the input data set for the inversion of dust particle parameters. On the other hand, for



1 particles with depolarization ratios of less than 30% the results obtained from  $3\beta+2\alpha$  and  
2  $3\beta+2\alpha+1\delta$  observations are in reasonable agreement and the use of the  $3\beta+2\alpha+1\delta$  dataset in the  
3 inversion of low depolarizing aerosols permits spheroids volume fraction to be estimated.

4 The analysis performed here also demonstrates the importance of the spectral dependence  
5 of the imaginary part of RI in the UV spectral region. Model simulations demonstrate that  
6 including  $m_I(\lambda)$  dependence may increase the values of effective radius and volume by a factor  
7 as large as 1.5. Thus, at the moment, dust particle microphysical properties obtained by inversion  
8 of lidar measurements may contain significant biases. Further research is needed to develop  
9 techniques correcting these biases in order the uncertainty of the estimates of  $r_{\text{eff}}$  and  $V$  to remain  
10 below 30%, which is a typical value when particles with prevailing fine mode are considered.

11 In addition to aerosol properties, the LILAS system provided profiles of the water vapor  
12 mixing ratio, which, being a conserved quantity, was frequently a convenient tracer that  
13 indicated the boundary between dry air masses transported over the continent and moist air  
14 masses transported over the ocean. The episodes considered in this paper were characterized  
15 mainly by low values of RH and the effects of the particles hygroscopic growth were not  
16 considered. Still, we have significant amount of the measurements in the condition of high RH,  
17 accompanied by formation of water and ice clouds near the dust layers. We plan to present these  
18 results in a separate publication.

19

20 **Acknowledgments:** The authors are very grateful to IRD-Dakar (Institut de Recherche pour le  
21 Développement) for their welcome and efficient support and also thank the labex CaPPA for  
22 supporting this campaign. The CaPPA project (Chemical and Physical Properties of the  
23 Atmosphere) is funded by the French National Research Agency (ANR) through the PIA  
24 (Programme d'Investissement d'Avenir) under contract "ANR-11-LABX-0005-01" and by the  
25 Regional Council "Nord-Pas de Calais" and the "European Funds for Regional Economic  
26 Development (FEDER)

27

28



## 1 **References**

- 2 Ansmann, A. and Müller, D.: Lidar and atmospheric aerosol particles, in “Lidar. Range-Resolved  
3 Optical Remote Sensing of the Atmosphere”, Weitkamp, C. ed., Springer, New York, 2005,  
4 pp. 105-141.
- 5 Ansmann, A., Petzold, A., Kandler, K., Tegen, I., Wendisch, M., Müller, D., Weinzierl, B.,  
6 Müller, T., Heintzenberg, J.: Saharan Mineral Dust Experiments SAMUM-1 and SAMUM-  
7 2: what have we learned?, *Tellus*, 63B, 403–429, 2011.
- 8 Ansmann, A., Seifert, P., Tesche, M., Wandinger, U.: Profiling of fine and coarse particle mass:  
9 case studies of Saharan dust and Eyjafjallajökull/Grimsvötn volcanic plumes. *Atmos. Chem.*  
10 *Phys.*, 12, 9399–9415, 2012.
- 11 Balkanski, Y., Schulz, M., Claquin, T., and Guibert, S.: Reevaluation of mineral aerosol radiative  
12 forcings suggests a better agreement with satellite and AERONET data, *Atmos. Chem. Phys.*,  
13 7, 81–95, 2007.
- 14 Biniotoglou, I., Basart, S., Alados-Arboledas, L., Amiridis, V., and co-authors: A methodology  
15 for investigating dust model performance using synergistic EARLINET/AERONET dust  
16 concentration retrievals. *Atmos. Meas. Tech.*, 8, 3577–3600, 2015.
- 17 Browning, K. A. and Wexler, R.: The determination of kinematic properties of a wind field using  
18 Doppler radar, *J. Appl. Meteor.*, 7, 105–113, 1968.
- 19 Burton, S. P., Vaughan, M. A., Ferrare, R. A. and Hostetler, C. A.: Separating mixtures of  
20 aerosol types in airborne High Spectral Resolution Lidar data. *Atmos. Meas. Tech.*, 7, 419–  
21 436, 2014.
- 22 De Tomasi, F., Blanco, A., and Perrone, M. R.: Raman lidar monitoring of extinction and  
23 backscattering of African dust layers and dust characterization. *Appl. Opt.* 42, 1699-1709,  
24 2003.
- 25 Di Girolamo, P., Summa, D., Bhawar, R., Di Iorio, T., Cacciani, M., Veselovskii, I., Dubovik,  
26 O., Kolgotin, A.: Raman lidar observations of a Saharan dust outbreak event:  
27 characterization of the dust optical properties and determination of particle size and  
28 microphysical parameters, *Atmospheric Environment*. 50, 66-78, 2012.
- 29 Dubovik, O., Sinyuk, A., Lapyonok, T., Holben, B.N., Mishchenko, M., Yang, P., Eck, T.F.,  
30 Volten, H., Munoz, O., Veihelmann, B., van der Zande, W.J., Leon, J.-F., Sorokin, M.,  
31 Slutsker, I.: Application of spheroid models to account for aerosol particle nonsphericity in



- 1 remote sensing of desert dust, *J. Geophys. Res.*, 111, D11208, doi:10.1029/2005JD006619,  
2 2006.
- 3 Esselborn, M., Wirth, M., Fix, A., Weinzierl, B., Rasp, K., Tesche, M., and Petzold, A.: Spatial  
4 distribution and optical properties of Saharan dust observed by airborne high spectral  
5 resolution lidar during SAMUM 2006, *Tellus B*, 61, 131–143, 2009.
- 6 Formenti, P., Schütz, L., Balkanski, Y., Desboeufs, K., Ebert, M., Kandler, K., Petzold, A.,  
7 Scheuvs, D., Weinbruch, S., and Zhang, D.: Recent progress in understanding physical and  
8 chemical properties of African and Asian mineral dust, *Atmos. Chem. Phys.*, 11, 8231–8256,  
9 doi:10.5194/acp-11-8231-2011, 2011.
- 10 Formenti P., A. Klaver, S. Chevaillier, E. Journet, J. Rajot, Mapping the physico-chemical  
11 properties of mineral dust in western Africa: mineralogical composition, *Atmos. Chem. Phys.*,  
12 14, 10663–1068, 2014.
- 13 Freudenthaler, V., Esselborn, M., Wiegner, M., Heese, B., Tesche, M. and co-authors:  
14 Depolarization ratio profiling at several wavelengths in pure Saharan dust during SAMUM  
15 2006, *Tellus B*, 61B, 165–179, 2009.
- 16 Gasteiger, J., Wiegner, M., Groß, S., Freudenthaler, V., Toledano, C., Tesche, M., and Kandler,  
17 K.: Modeling lidar-relevant optical properties of complex mineral dust aerosols, *Tellus B*,  
18 63, 725–741, 2011.
- 19 Kandler, K., Lieke, K., Benker, N., Emmel, C., Küpper, M., Müller-Ebert, D., Ebert, M.,  
20 Scheuvs, D., Schladitz, A., Schütz, L., Weinbruch, S.: Electron microscopy of particles  
21 collected at Praia, Cape Verde, during the Saharan Mineral Dust Experiment: Particle  
22 chemistry, shape, mixing state and complex refractive index. *Tellus B*, 475–496, 2011.
- 23 Klett J.D., “Lidar inversion with variable backscatter/extinction ratios”, *Appl. Opt.* 24, 1638–  
24 1643, 1985.
- 25 Kumer, V.-M., Reuder, J., Furevik, B.R.: A comparison of LiDAR and radiosonde wind  
26 measurements, *Energy Procedia*, 53, 214–220, 2014.
- 27 Li, W. J., and Shao, L. Y.: Observation of nitrate coatings on atmospheric mineral dust particles  
28 *Atmos. Chem. Phys.*, 9, 1863–1871, 2009.
- 29 Mahowald, N. M., Kloster, S., Engelstaedter, S., Moore, J. K., Mukhopadhyay, S., McConnell, J.  
30 R., Albani, S., Doney, S. C., Bhattacharya, A., Curran, M. A. J., Flanner, M. G., Hoffman, F.  
31 M., Lawrence, D. M., Lindsay, K., Mayewski, P. A., Neff, J., Rothenberg, D., Thomas, E.,



- 1 Thornton, P. E., and Zender, C. S.: Observed 20th century desert dust variability: impact on  
2 climate and biogeochemistry, *Atmos.Chem. Phys.*, 10, 10875-10893, 2010.
- 3 McConnell, C. L., Highwood, E. J., Coe, H., Formenti, P., Anderson, Osborne, B. S., Nava, S.,  
4 Desboeufs, K., Chen, G., Harrison, M. A. J.: Seasonal variations of the physical and optical  
5 characteristics of Saharan dust: results from the Dust Outflow and Deposition to the Ocean  
6 (DODO) experiment, *J. Geophys. Res.* **113**, D14S05, doi:10.1029/2007JD009606, 2008.
- 7 Mishchenko, M.I., L.D. Travis, R.A. Kahn, and R.A. West, Modeling phase functions for  
8 dustlike tropospheric aerosols using a mixture of randomly oriented polydisperse spheroids,  
9 *J. Geophys. Res.*, Vol. 102, 16831-16847, 1997
- 10 Mona, L., Amodeo, A., Pandolfi, M., Pappalardo, G.: Saharan dust intrusions in the  
11 Mediterranean area: three years of Raman lidar measurements. *J. Geophys. Res.*, 111,  
12 D16203, doi:10.1029/2005JD006569, 2006.
- 13 Müller, D., Wandinger, U., and Ansmann, A.: Microphysical particle parameters from extinction  
14 and backscatter lidar data by inversion with regularization: theory, *Appl. Opt.* 38, 2346-2357,  
15 1999.
- 16 Müller, D., Mattis, I., Wandinger, U., Ansmann, A., Althausen, D., Stohl, A.: Raman lidar  
17 observations of aged Siberian and Canadian forest fire smoke in the free troposphere over  
18 Germany in 2003: Microphysical particle characterization, *J. Geophys. Res.*, 110, D17201,  
19 doi:10.1029/2004JD005756, 2005.
- 20 Müller, D., Weinzierl, B., Petzold, A., Kandler, K., Ansmann, A., Müller, T., Tesche, M.,  
21 Freudenthaler, V., Esselborn, M., Heese, B., Althausen, D., Schladitz, A., Otto, S., and  
22 Knippertz, P.: Mineral dust observed with AERONET Sun photometer, Raman lidar and in  
23 situ instruments during SAMUM 2006: shape-independent particle properties, *J. Geophys.*  
24 *Res.*, 115, D11207, doi:10.1029/2009JD012523, 2010.
- 25 Müller, D., Veselovskii, I., Kolgotin, A., Tesche, M., Ansmann, A., Dubovik, O.: Vertical  
26 profiles of pure dust (SAMUM-1) and mixed smoke-dust plumes (SAMUM-2) inferred from  
27 inversion of multiwavelength Raman/polarization lidar data and comparison to AERONET  
28 retrievals and in-situ observations, *Appl.Opt.* 52, 3178-3202, 2013.
- 29 Nisantzi, A., Mamouri, R. E., Ansmann, A., Schuster, G. L., Hadjimitsis, D. G.: Middle East  
30 versus Saharan dust extinction-to-backscatter ratios. *Atmos. Chem. Phys.*, 15, 7071–7084,  
31 2015.



- 1 Papayannis, A., Amiridis, V., Mona, L., Tsaknakis, G., Balis, D., Bösenberg, J., Chaikovski, A.,  
2 De Tomasi, F., Grigorov, I., Mattis, I., Mitev, V., Müller, D., Nickovic, S., Pérez, C.,  
3 Pietruczuk, A., Pisani, G., Ravetta, F., Rizi, V., Sicard, M., Trickl, T., Wiegner, M.,  
4 Gerding, M., Mamouri, R. E., D'Amico, G., and Pappalardo, G.: Systematic lidar  
5 observations of Saharan dust over Europe in the frame of EARLINET (2000–2002), *J.*  
6 *Geophys. Res.*, 113, D10204, doi:10.1029/2007JD009028, 2008.
- 7 Papayannis, A., Mamouri, R. E., Amiridis, V., Remoundaki, E., Tsaknakis, G., Kokkalis, P.,  
8 Veselovskii, I., Kolgotin, A., Nenes, A., and Fountoukis, C.: Optical-microphysical  
9 properties of Saharan dust aerosols and composition relationship using a multi-wavelength  
10 Raman lidar, in situ sensors and modelling: a case study analysis, *Atmos. Chem. Phys.* 12,  
11 4011-4032 (2012).
- 12 Patterson, E.M., Gillette, D.A., Stockton, B.H.: Complex Index of Refraction Between 300 and  
13 700 nm for Saharan Aerosols, *J. Geophys. Res.* 82, 3153 - 3160, 1977.
- 14 Redelsperger, J.-L., Thorncroft, C. D., Diedhiou, A., Lebel, T., Parker, D. J., Polcher, J.: African  
15 Monsoon Multidisciplinary Analysis: an international research project and field campaign.  
16 *Bull. Am.Meteorol. Soc.* 87, 1739–1746, 2006.
- 17 Reid, J. S. and Maring, H. B: Foreword to special section on the Puerto Rico Dust Experiment  
18 (PRIDE), *J. Geophys. Res.* 108, 8585, doi:10.1029/2003JD003510, 2003.
- 19 Ruchith, R.D. and Ernest Raj, P.: Features of nocturnal low level jet (NLLJ) observed over a  
20 tropical Indian station using high resolution Doppler wind lidar, *Journal of Atmospheric and*  
21 *Solar-Terrestrial Physics*, 123, 113-123, 2015.
- 22 Sakai, T., Nagai, T., Nakazato, M., Mano, Y., and Matsumura, T: Ice clouds and Asian dust studied  
23 with lidar measurements of particle extinction-to-backscatter ratio, particle depolarization,  
24 and water-vapor mixing ratio over Tsukuba. *Appl.Opt.* 42, 7103-7116, 2003.
- 25 Seibert, P., Beyrich, F., Gryning S., Joffre, S., Rasmussen, A., Tercier, P.: Review and  
26 intercomparison of operational methods for the determination of the mixing height,  
27 *Atmospheric Environment*, 34, 1001–1027, 2000.
- 28 Shimizu, A., Sugimoto, N., Matsui, I., Arao, K., Uno, I., Murayama, T., Kagawa, N., Aoki, K.,  
29 Uchiyama, A., Yamazaki, A.: Continuous observations of Asian dust and other aerosols by  
30 polarization lidars in China and Japan during ACE-Asia, *J. Geophys. Res.*, 109, D19S17,  
31 doi:10.1029/2002JD003253, 2004.



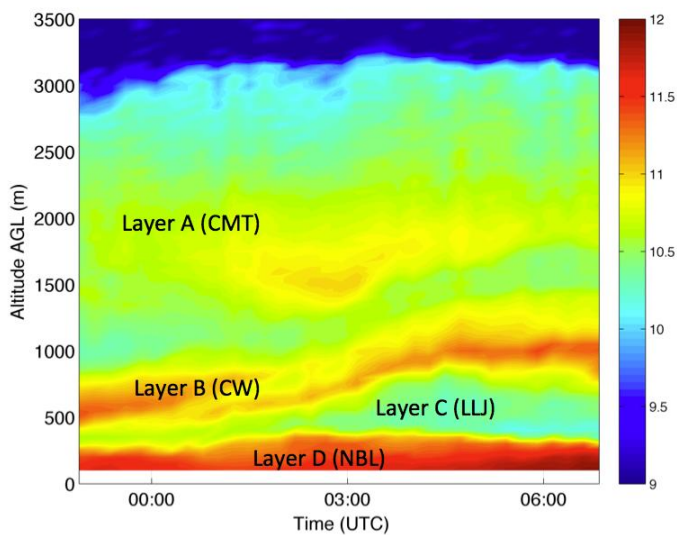
- 1 Sokolik, I. N. and Toon, O. B.: Direct radiative forcing by anthropogenic airborne mineral  
2 aerosols, *Nature*, 381, 681–683, 1996.
- 3 Tanre, D., Haywood, J., Pelon, J., Leon, J.-F., Chatenet, B., Formenti, P., Francis, P., Goloub, P.,  
4 Highwood, E. J., Myhre, G.: Measurements and modeling of the Saharan dust radiative  
5 impact: overview of the Saharan Dust Experiment (SHADE). *J. Geophys. Res.* 108, 8574,  
6 doi:10.1029/2002JD003273, 2003.
- 7 Tesche, M., Ansmann, A., Müller, D., Althausen, D., Engelmann, R., Freudenthaler, V., and  
8 Groß, S.: Vertically resolved separation of dust and smoke over Cape Verde using  
9 multiwavelength Raman and polarization lidars during Saharan Mineral Dust Experiment  
10 2008, *J. Geophys. Res.*, 114, D13202, doi:10.1029/2009JD011862, 2009a.
- 11 Tesche, M., Ansmann, A., Müller, D., Althausen, D., Mattis, I., Heese, B., Freudenthaler, V.,  
12 Wiegner, M., Eeseborn, M., Pisani, G., and Knippertz, P.: Vertical profiling of Saharan dust  
13 with Raman lidars and airborne HSRL in southern Morocco during SAMUM, *Tellus B*, 61,  
14 144–164, doi:10.1111/j.1600-0889.2008.00390.x, 2009b.
- 15 Tesche, M., Groß, S., Ansmann, A., Müller, D., Althausen, D., Freudenthaler, V., and Esselborn,  
16 M.: Profiling of Saharan dust and biomass-burning smoke with multiwavelength  
17 polarization Raman lidar at Cape Verde, *Tellus B*, 63, 649–676, doi:10.1111/j.1600-  
18 0889.2011.00548.x, 2011.
- 19 Thobois, L. and Soderholm, J.: Observing clear air close proximity environment of severe  
20 storms, *Meteorological Technology International*, 9, 132-135, 2015.
- 21 Veselovskii I., Kolgotin, A., Griaznov, V., Müller, D., Wandinger, U., Whiteman, D.:  
22 Inversion with regularization for the retrieval of tropospheric aerosol parameters from multi-  
23 wavelength lidar sounding, *Appl. Opt.* 41, 3685-3699, 2002.
- 24 Veselovskii I., O. Dubovik, A. Kolgotin, T. Lapyonok, P. Di Girolamo, D. Summa, D. N.  
25 Whiteman, M. Mishchenko, and D. Tanré, 2010: Application Of Randomly Oriented  
26 Spheroids For Retrieval Of Dust Particle Parameters From Multiwavelength Lidar  
27 Measurements, *J. Geophys. Res.*, **115**, D21203, doi:10.1029/2010JD014139, 2010.
- 28 Veselovskii, I., Whiteman, D. N., Korenskiy, M., Suvorina, A., Kolgotin, A., Lyapustin, A.,  
29 Wang, Y., Chin, M., Bian, H. Kucsera, T. L., Perez-Ramirez, D., Holben, B.:  
30 Characterization of forest fire smoke event near Washington, D.C. in Summer 2013 with  
31 multi-wavelength lidar. *Atmos. Chem. Phys.* 15, 1647–1660, 2015.



- 1 Veselovskii, I., Whiteman, D. N., Korenskiy, M., Suvorina, A., Perez-Ramirez, D.: Use of  
2 rotational Raman measurements in multiwavelength aerosol lidar for evaluation of particle  
3 backscattering and extinction, *Atmos. Meas. Tech.*, 8, 4111–4122, 2015.
- 4 Wagner, J., Ansmann, A., Wandinger, U., Seifert, P., Schwarz, A., Tesche, M., Chaikovsky, A.,  
5 Dubovik, O.: Evaluation of the Lidar/Radiometer Inversion Code (LIRIC) to determine  
6 microphysical properties of volcanic and desert dust, *Atmos. Meas. Tech.*, 6, 1707–1724,  
7 2013.
- 8 Whiteman, D., Melfi, S., Ferrare, R.: Raman lidar system for measurement of water vapor and  
9 aerosols in the Earth's atmosphere", *Appl. Opt.* 31, 3068-3082, 1992.
- 10 Wiegner, M., Gasteiger, J., Kandler, K., Weinzierl, B., Rasp, K., Esselborn, M., Freudenthaler,  
11 V., Heese, B., Toledano, C., Tesche, M., Althausen, D.: Numerical simulations of optical  
12 properties of Saharan dust aerosols with emphasis on lidar applications. *Tellus* 61B, 180–  
13 194, 2009.
- 14 Xie, C., Nishizawa, T., Sugimoto, N., Matsui, I., and Wang, Z.: Characteristics of aerosol optical  
15 properties in pollution and Asian dust episodes over Beijing, China. *Appl. Opt.* 47, 4945-  
16 4951, 2008.
- 17
- 18



1



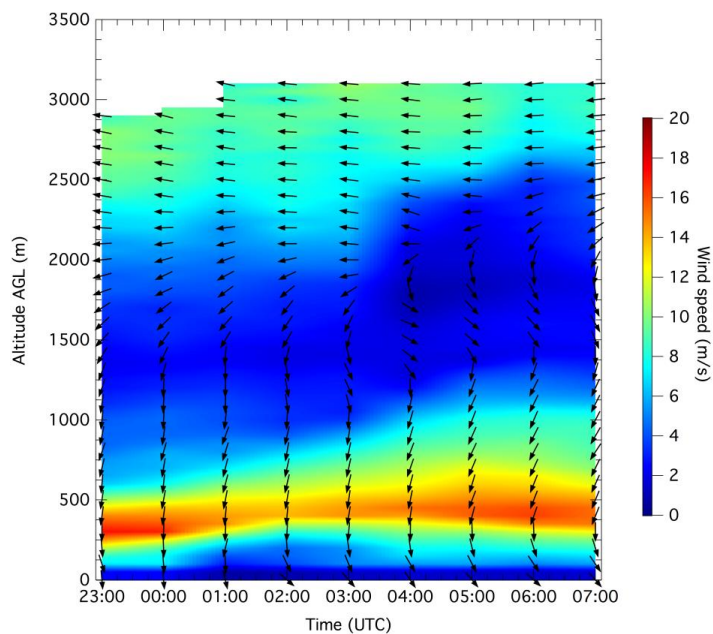
2

3 Fig.1. Time-height section of the logarithmic range corrected lidar signal deduced from the  
4 Doppler lidar measurements during the 15-16 April night at Mbour. The stratification is  
5 represented by four layers: (A) continentalized maritime trade (CMT), (B) Layer advected  
6 mainly by a continental wind (CW), (C) low-level jet (LLJ) and (D) nocturnal boundary layer  
7 (NBL).

8



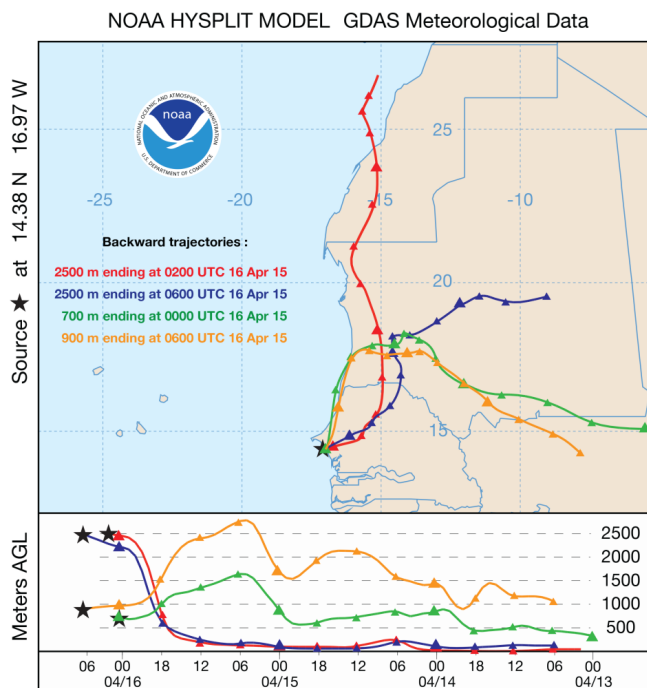
1



2  
3  
4

5 Fig. 2. Time-height section of wind direction (arrows) and wind speed (color map) deduced from  
6 Doppler lidar during 15-16 April. Leftward and downward arrows represent, respectively,  
7 easterly wind and northerly wind

8



1

2 Fig.3. Back trajectories of the air masses ending in Mbour on 16 April 2015 at 2500 m (02:00  
3 UTC, 06:00 UTC), at 900 m (00:00 UTC) and at 700 m (06:00 UTC).

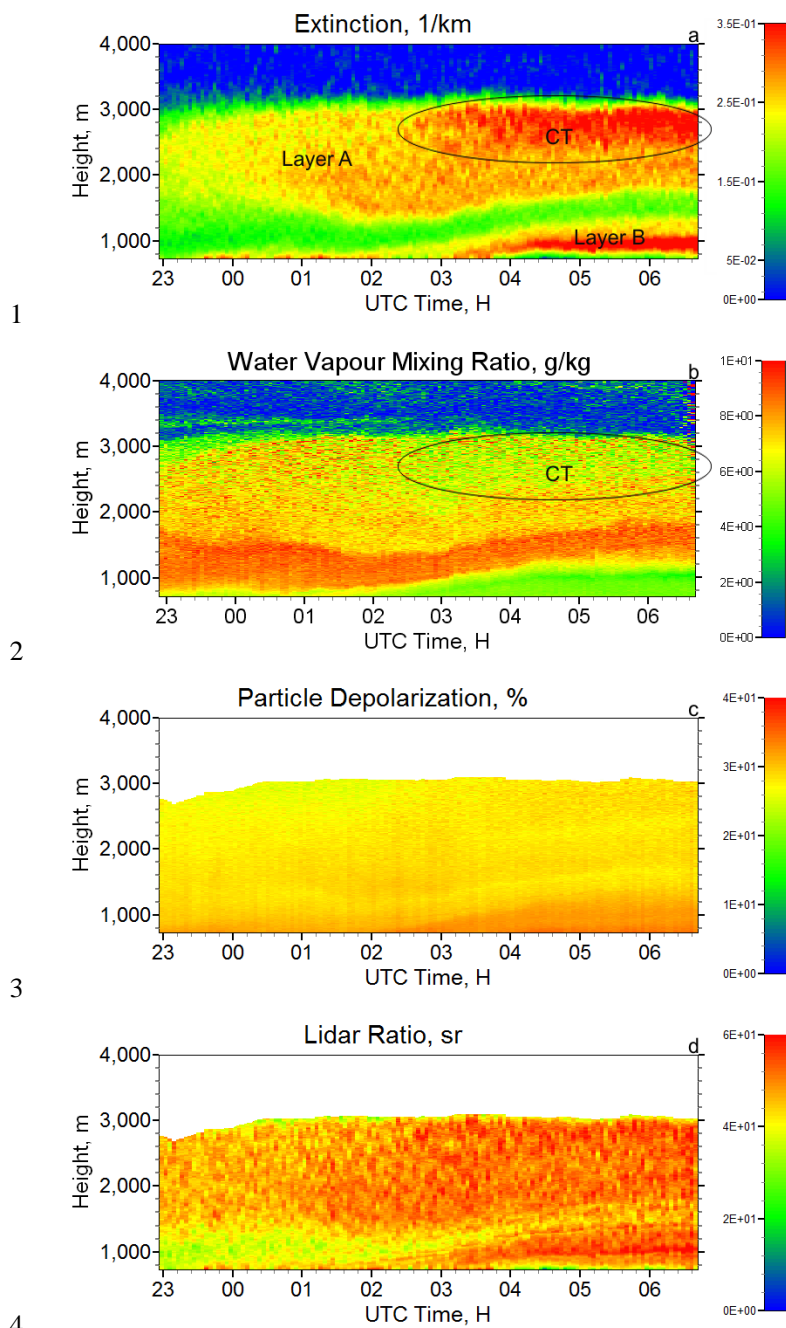
4

5

6

7

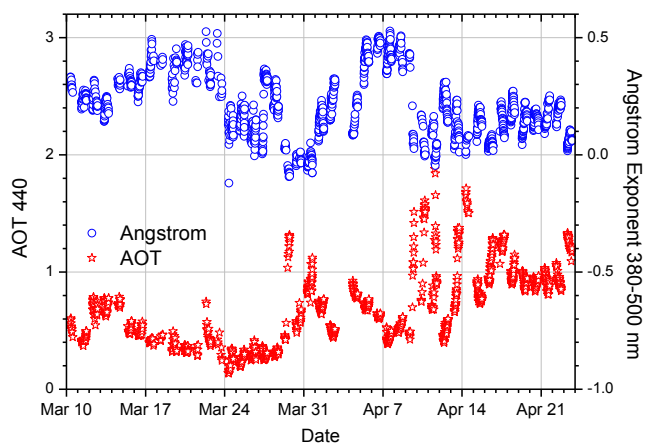
8



5 Fig.4. Height-temporal distribution of particle characteristics: (a) extinction  $\alpha_{532}$ , (b) water vapor  
6 mixing ratio, (c) particle depolarization and (d) lidar ratio  $R_{532}$  measured during the 15-16 April  
7 night.

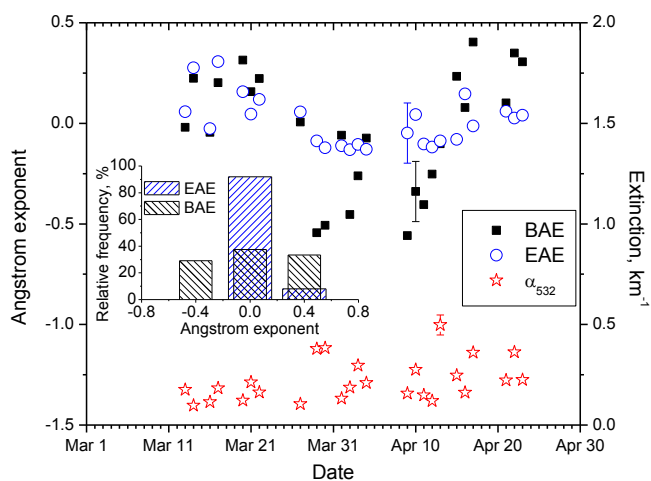


1  
2



3  
4  
5  
6  
7

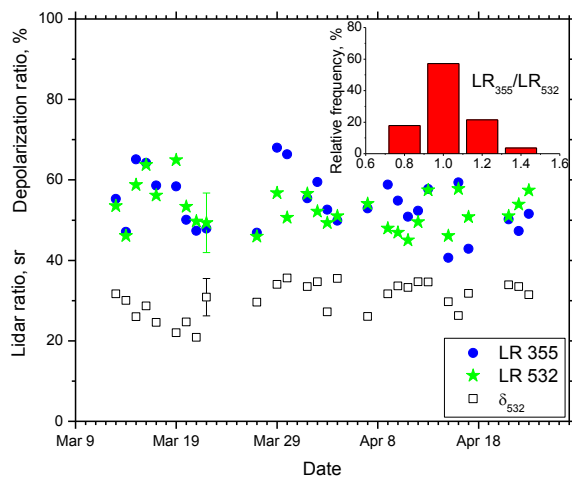
Fig.5. Aerosol optical thickness (AOT) at 440 nm and the extinction Ångström exponent at 380-550 nm wavelengths provided by AERONET in Mbour for March – April 2015 period.



1

2 Fig. 6. Particle extinction at 532 nm together with backscattering and extinction Ångström  
 3 exponents derived from lidar measurements within 1500 m – 2000 m layer for period March-  
 4 April 2015. The insert shows the frequency distributions of BAE and EAE.

5



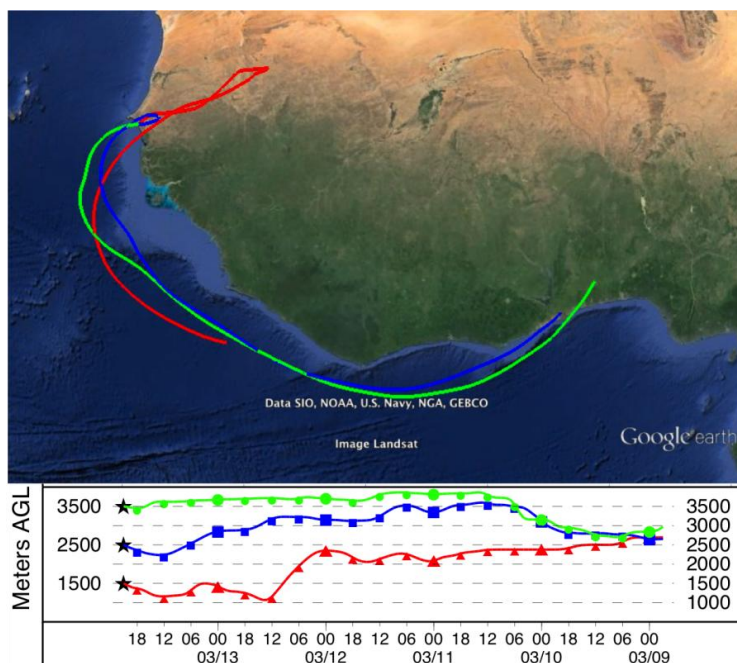
6

7 Fig. 7. Lidar ratios at 355 nm and 532 nm together with particle depolarization ratios derived  
 8 from lidar measurements within 1500 m – 2000 m layer for period March-April 2015. The insert  
 9 shows the frequency distribution of the ratio  $LR_{355}/LR_{532}$ .



1

2



3

4

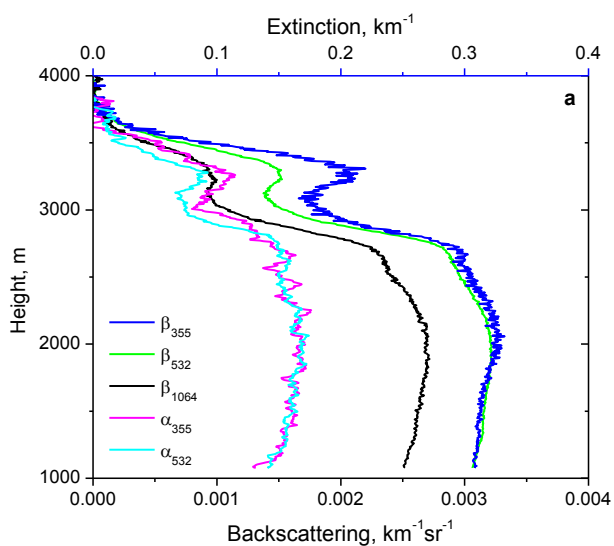
5 Fig.8. Five-day backward trajectories for the air mass in Mbour at altitudes 1500 m, 2500 m,  
6 3500 m, on 13 March 2015 at 21:00 UTC.

7

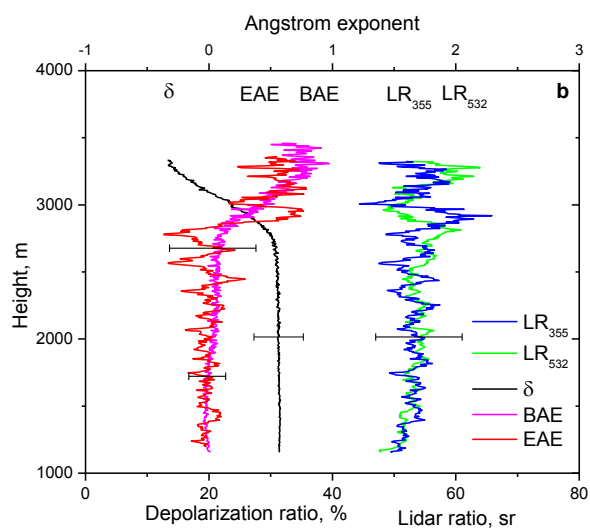
8

9

10



1



2

3 Fig.9. Vertical profiles of (a) backscattering and extinction coefficients and (b) lidar ratios,  
4 depolarization ratio, backscattering and extinction Ångström exponents at 355/532 nm measured  
5 on 13 March 2015 for period 20:30-21:30 UTC.

6

7

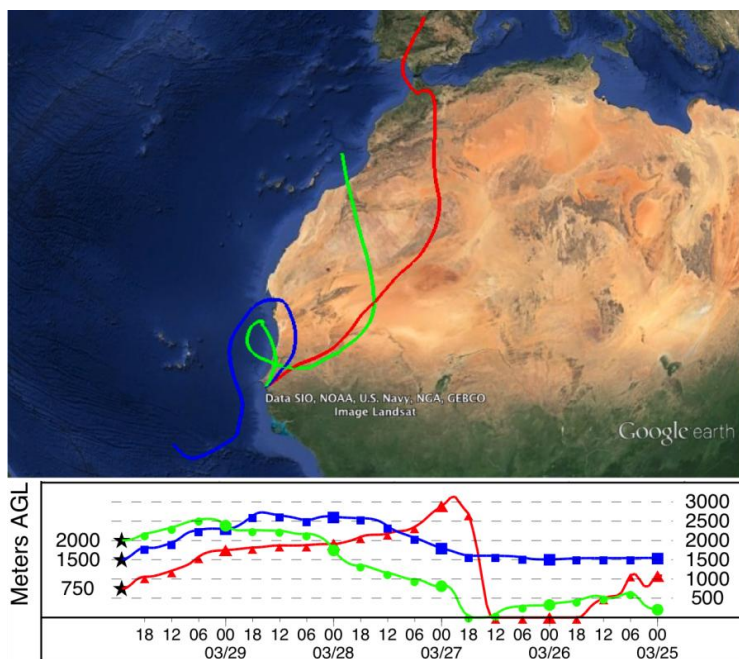
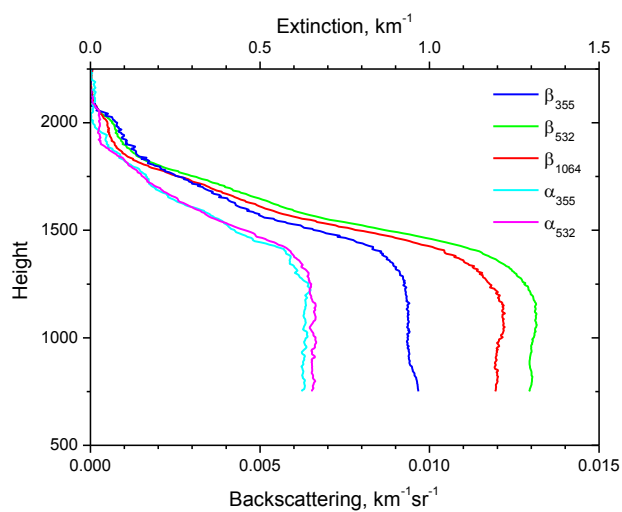


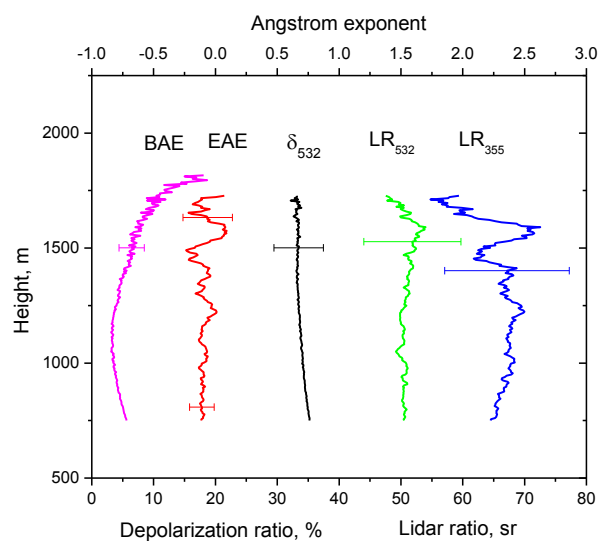
Fig.10. Five-day backward trajectories for the air mass in Mbour at altitudes 750 m, 1500 m, 2000 m on 29 March 2015 at 23:00 UTC.



1



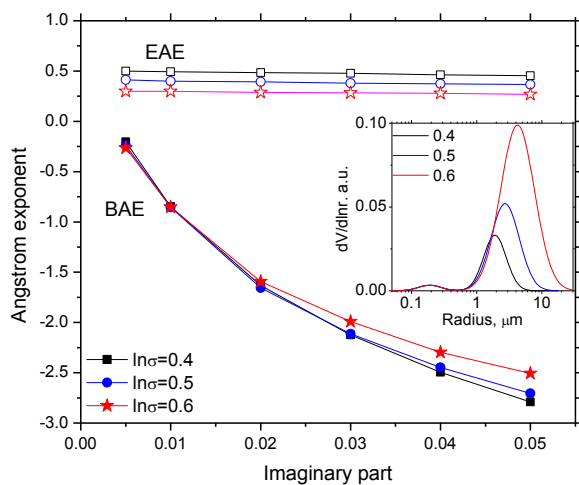
2



3

4 Fig.11. Vertical profiles of (a) backscattering and extinction coefficients,  
5 depolarization ratio, backscattering and extinction Ångström exponents measured on 29 March  
6 2015 for period 22:00-23:30 UTC.

7



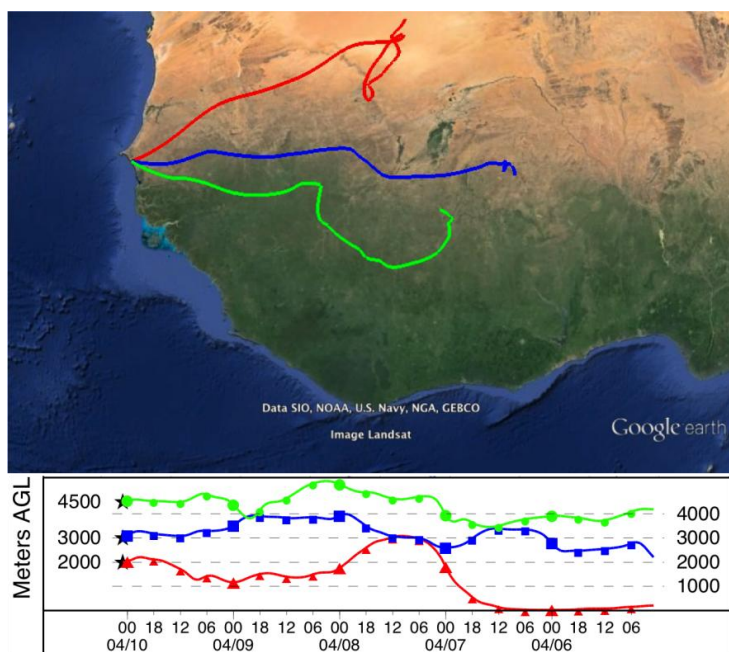
1

2 Fig.12. Extinction and backscattering Ångström exponent for 355/532nm wavelengths as a  
3 function of the imaginary part of the refractive index at 355 nm. The CRI at 532 nm was kept  
4  $m=1.55-i.005$ . Computations were performed using the model of randomly oriented spheroids  
5 for three bimodal PSDs shown in the insert.

6



1



2

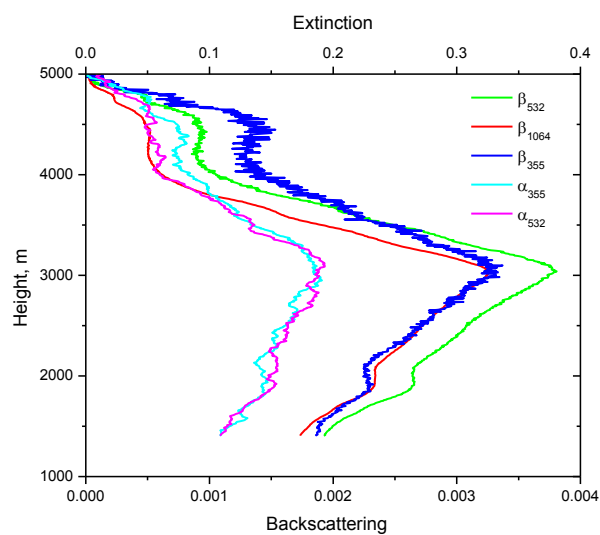
3

4 Fig.13. Five-day backward trajectories for the air mass in Mbour at altitudes 2000 m, 3000 m,  
5 4500 m on 10 April 2015 at 01:00 UTC.

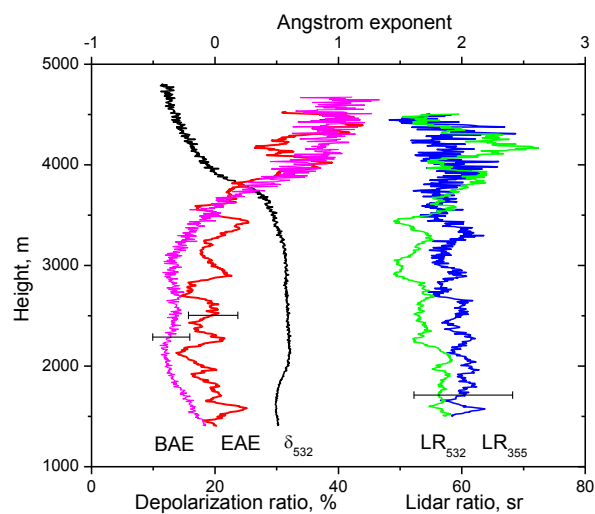
6



1



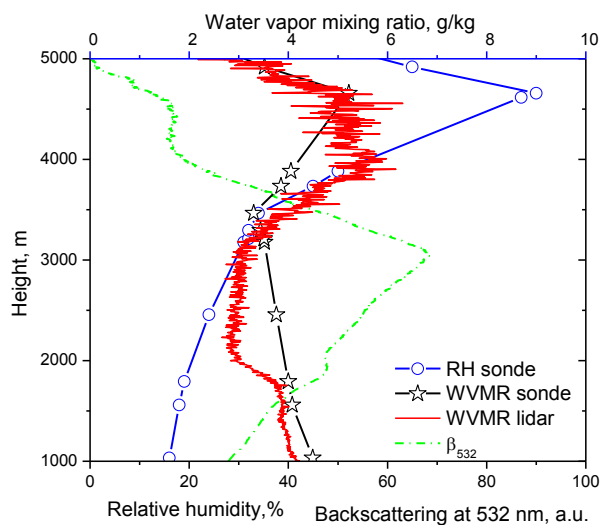
2



3

4

5 Fig.14 Vertical profiles of (a) backscattering and extinction coefficients and (b) depolarization  
6 ratio, backscattering and extinction Ångström exponents measured on 10 April 2015 for period  
7 00:00-02:00 UTC. Open symbols show the relative humidity and WVMR from midnight  
8 radiosond measurements in Dakar.



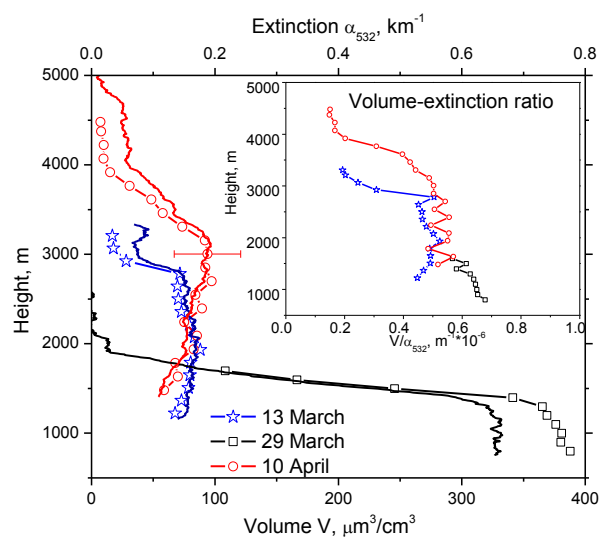
1

- 2 Fig.15. Vertical profile of water vapor mixing ratio (WVMR) measured with Raman lidar. The  
3 symbols show WVMR and the relative humidity (RH) measured with radio sonde in Dakar on 10  
4 April at 00:00 UTC. Green dash-dot line shows backscattering coefficient at 532 nm.



1

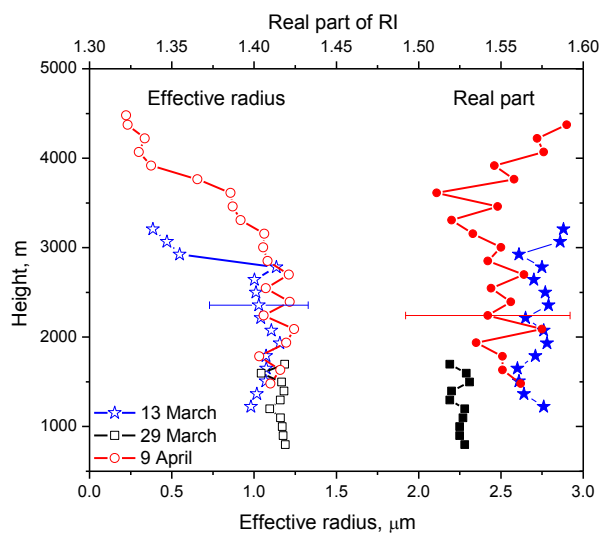
2



3

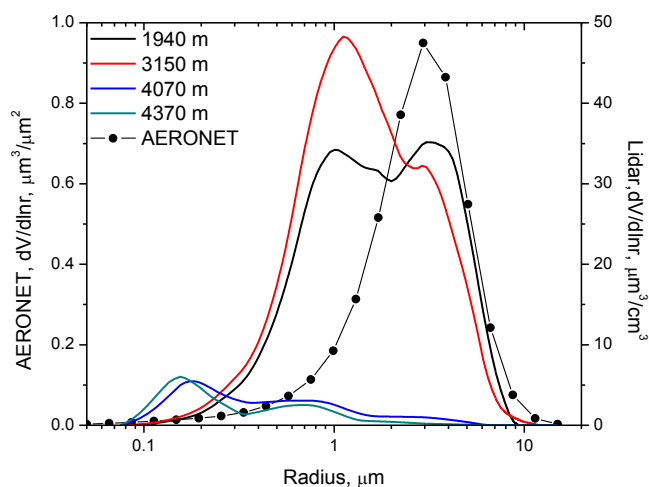
4 Fig.16. Vertical profiles of the particle volume density  $V$  retrieved from  $3\beta+2\alpha$  measurements on  
5 13 March, 29 March and 10 April (symbols). Solid lines indicate the profiles of extinction  
6 coefficient at 532 nm. The insert shows the volume – extinction ratio  $V/\alpha_{532}$  for the days  
7 considered.

8

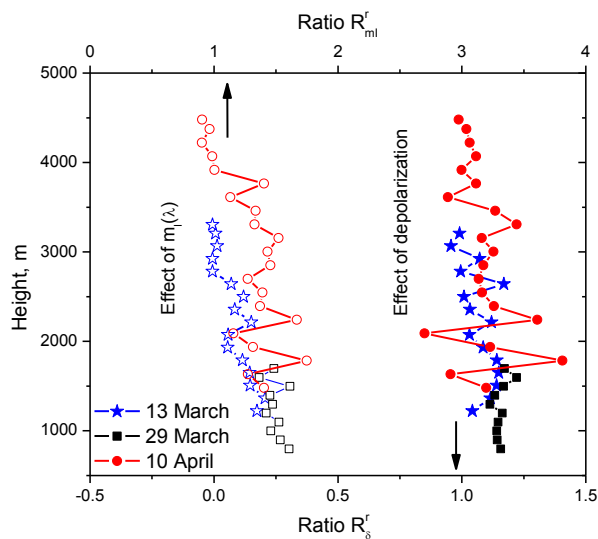


1

2 Fig.17. The profiles of (open symbols) the particle effective radius and (solid symbols) the real  
3 part of RI retrieved from  $3\beta+2\alpha$  measurements on 13 March, 29 March and 10 April.



1  
 2 Fig.18. Particle size distributions retrieved from the measurements on 10 April for four height  
 3 layers 1940, 3150, 4070, 4370 m. Symbols show the PSD provided by AERONET on 9 April at  
 4 18:00 UTC, inversion level 1.5.



5  
 6 Fig. 19. Enhancement of retrieved effective radius due to using the particle depolarization ratio  
 7 in input data set ( $R_s^r$ ) and due to accounting for the spectral dependence of the imaginary part of  
 8 RI ( $R_m^r$ ). Shown are results for the measurements on 13 March, 29 March and 10 April 2015.